

Does the i-process operate at nearly solar metallicity?

D. Karinkuzhi^{1,2}, S. Van Eck², S. Goriely², L. Siess², A. Jorissen², A. Choplin², A. Escorza³, S. Shetye⁴, and H. Van Winckel⁵

¹ Department of Physics, University of Calicut, Thenhipalam, Malappuram 673635, India

² Institut d'Astronomie et d'Astrophysique, Université Libre de Bruxelles (ULB) C.P. 226, B-1050 Bruxelles, Belgium

³ European Southern Observatory, Alonso de Córdova 3107, Vitacura, Casilla 19001, Santiago de Chile, Chile

⁴ Institute of Physics, Laboratory of Astrophysics, École polytechnique fédérale de Lausanne (EPFL), Observatoire de Sauverny, 1290 Versoix, Switzerland

⁵ Instituut voor Sterrenkunde, KULeuven, Celestijnenlaan 200D, 3001 Leuven, Belgium

Received X, 2023; accepted Y, 2023

ABSTRACT

Context. A sample of 895 s-process-rich candidates has been found among the 454 180 giant stars surveyed by LAMOST at low spectral resolution ($R \sim 1800$). In a previous study, taking advantage of the higher resolution ($R \sim 86\,000$) offered by the HERMES-Mercator spectrograph, we performed the re-analysis of 15 among the brightest stars of this sample. Among these 15 programme stars, having close-to-solar metallicities, 11 showed mild to strong heavy element overabundances. The nucleosynthetic process(es) at the origin of these overabundances were however not questioned in our former study.

Aims. We derive the abundances in s- and r-process elements of the 15 targets in order to investigate whether some stars also show an i-process signature, as sometimes found in their lower metallicity counterparts (namely, the Carbon-Enhanced Metal-Poor (CEMP)-rs stars).

Methods. Abundances are derived from the high-resolution HERMES spectra for Pr, Nd, Sm, and Eu, using the TURBOSPECTRUM radiative transfer LTE code with MARCS model atmospheres.

Results. Using the new classification scheme proposed in our recent study we find that two stars show overabundances in both s- and r-process elements well above the level expected from the Galactic chemical evolution, an analogous situation to the one of CEMP-rs stars at lower metallicities. We compare the abundances of the most enriched stars with the nucleosynthetic predictions from the STAREVOL stellar evolutionary code and find abundances compatible with an i-process occurring in AGB stars.

Conclusions. Despite a larger number of heavy elements to characterize the enrichment pattern, the limit between CEMP-s and CEMP-rs stars remains fuzzy. It is however interesting to note that an increasing number of extrinsic stars are found to have abundances better reproduced by an i-process pattern even at close-to-solar metallicities.

Key words. Nuclear reactions, nucleosynthesis, abundances – Stars: AGB and post-AGB – binaries: spectroscopic

1. Introduction

The origin of the peculiar chemical composition of CEMP-rs stars (carbon-enhanced-metal-poor stars enriched in *both* s and r elements) is an unsolved problem. Some of the scenarios that have been invoked to explain their overabundances (Jonsell et al. 2006; Masseron et al. 2010; Hampel et al. 2016) include (i) a primordial origin (the pollution of the birth cloud by an r-process source), (ii) a pollution of the binary by a third massive star (triple system), (iii) a pollution by the primary (type 1.5 supernova or accretion-induced collapse), or finally, (iv) the intermediate neutron-capture process or i-process. This nucleosynthesis process leads to neutron densities of the order of $N_n \sim 10^{15} \text{ cm}^{-3}$, intermediate between those of the s-process ($N_n \sim 10^8 \text{ cm}^{-3}$) and those required by the r-process ($N_n \gg 10^{20} \text{ cm}^{-3}$). Recently, Karinkuzhi et al. (2021a) studied a sample of CEMP-s and rs stars in our Galaxy and suggested that the abundance pattern in CEMP-rs stars can be produced by a TP-AGB star experiencing i-process nucleosynthesis after proton ingestion during its first convective thermal pulse, and transferring this material to a close-by companion. From a comparison of the abundance profiles of CEMP-s and CEMP-rs stars, Karinkuzhi et al. (2021a) noticed an abundance continuum rather than dichotomic

patterns. Hence, the i-process could be a manifestation of the s-process at low ($[\text{Fe}/\text{H}] \sim -2$) metallicities, when proton injection takes place. Our previous identification and analysis (Karinkuzhi et al. 2018) of a star enriched in s and r elements at higher metallicity ($[\text{Fe}/\text{H}] \sim -0.7$) hints at an i-process which would not be limited to metal-poor environments. The literature contains other pieces of evidence in that direction, such as the barium star subsamples of Cui et al. (2014) and den Hartogh et al. (2022), and the born-again phase of the *Sakurai* object which also seems to display an i-process pattern (Herwig et al. 2011). These observations show that it seems to be possible for a given object to produce this rs pattern without resorting to a "two-event" scenario (independent and cumulative pollutions by an r-process and an s-process).

In this paper we use sample of 15 stars from Norfolk et al. (2019) reanalyzed in Karinkuzhi et al. (2021b, hereafter K21) to check for potential hybrid profiles at close-to-solar metallicities. This paper is organized as follows. Section 2 describes the sample selection and Sect. 3 the method used to derive the atmospheric parameters and abundances. In Section 4 we classify the stars on the basis of their [s/r] ratio, while in Sect. 5 we use a classification based on a larger number of heavy elements. Section 6 presents AGB models and nucleosynthesis

reproducing the measured abundances with an i-process, triggered by a proton-injection episode (PIE) very similar to the one found in metal-poor stellar models. In Section 7 we show that the i-process provides a better agreement with the measured abundances than a superposition of two independent s- and r-pollutions. Conclusions are presented in Sect. 8.

2. Sample selection

Our sample consists in 15 bright barium stars selected from the 895 objects from Norfolk et al. (2019) and for which high-resolution HERMES (Raskin et al. 2011) spectra could be obtained. A first analysis of this sample was presented in K21. The metallicities range from $[\text{Fe}/\text{H}] = 0.02$ to -0.61 . Among the 15 programme stars, 4 show no s-process overabundances ($[\text{X}/\text{Fe}] < 0.2$ dex), 8 show mild s-process overabundances (at least three heavy elements with $0.2 \leq [\text{X}/\text{Fe}] < 0.8$), and 3 have strong overabundances (at least three heavy elements with $[\text{X}/\text{Fe}] \geq 0.8$), as listed in Table. 1.

The binarity of these stars was investigated by K21 from which it appears that 2 out of the 3 strong barium stars show a clear binary signature from radial-velocity (RV) variations. The results for the other classes are intriguing, however, since only 1 out of the 8 mild barium stars diagnosed exhibit statistically significant RV variations, and on the opposite, 2 out of the 4 ‘no-s’ stars show a binary signature.

3. Derivation of atmospheric parameters and abundances

The atmospheric parameter derivation is presented in K21. The stellar parameters are repeated here (Table 1).

Abundances were derived through spectral synthesis using the LTE TURBOSPECTRUM code (Alvarez & Plez 1998). We used solar abundances from Asplund et al. (2009) and the line lists of Heiter et al. (2015); Heiter (2020) as in Karinkuzhi et al. (2018, 2021a). Table A.1 presents the derived Pr, Nd, Sm, and Eu abundances, while we refer to Tables A.1 and A.2 of K21 for the remaining abundances. The complete abundance profiles are also presented in Fig. B.1 and B.2. Mashonkina et al. (2000) and Mashonkina & Christlieb (2014) studied the NLTE corrections for the Eu II 6645.135 Å line and showed that they are negligible (≈ 0.06 to 0.08 dex for metallicities higher than -3.0). For the other elements, we could not find information about NLTE corrections at the metallicities of our objects. The isotopic shifts and hyperfine splitting (HFS) of the atomic lines have been included while deriving the Eu abundances. For other elements the isotopic shifts and HFS splitting are not available for the lines we used. Fig. 1 presents the spectral fitting of Eu lines in a few sample stars. Though many Nd lines are available throughout the spectral coverage, we used the Nd II lines in the range 5200 – 5400 Å since they are relatively free from molecular blends. For Pr and Sm, we used all the measurable lines as listed in Karinkuzhi et al. (2018, 2021a). The details about the error estimates are presented in K21. The resulting changes in the abundances by varying the atmospheric parameters T_{eff} , $\log g$, micro-turbulence ξ , and $[\text{Fe}/\text{H}]$ by 100 K, 0.5, 0.5 km/s and 0.5 dex, respectively are presented in Table 2. The final errors are calculated using Eqs. 1 and 2 of K21 and are presented in Table A.1.

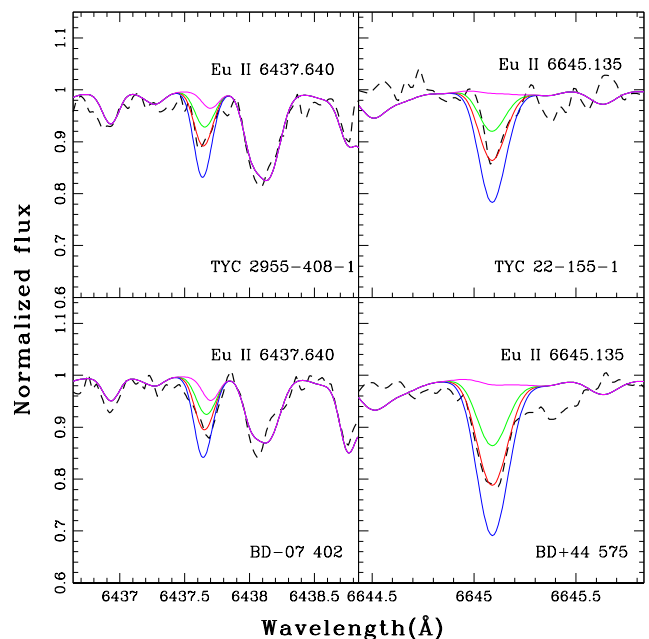


Fig. 1. Spectral fitting of the 6437.640 and 6645.135 Å Eu II lines for four sample stars. Red lines correspond to spectral syntheses with the abundance for Eu listed in Table A.1. Blue and green lines represent syntheses with abundances deviating by ± 0.3 dex from the adopted abundance. The magenta line corresponds to the synthesis with a null abundance for Eu.

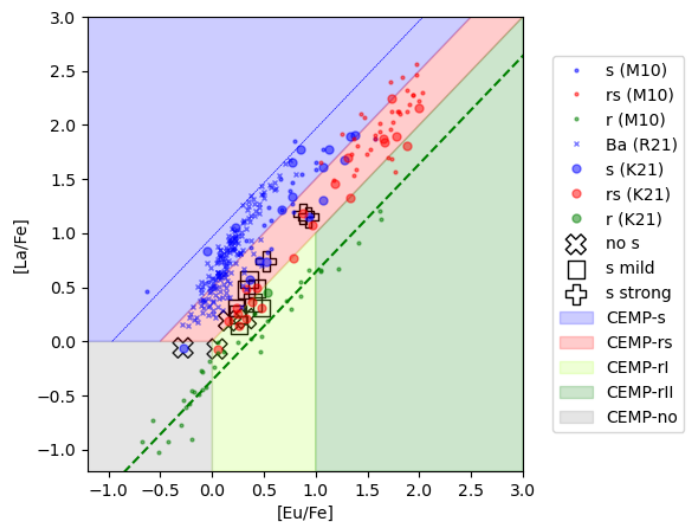


Fig. 2. $[\text{La}/\text{Fe}]$ as a function of $[\text{Eu}/\text{Fe}]$. CEMP-s stars, CEMP-rs stars, and r-process enriched stars from Masseron et al. (2010) and Karinkuzhi et al. (2018, 2021a) as well as the Ba stars of Roriz et al. (2021) are included in the figure. The dashed green line corresponds to abundance-ratio scaling with a pure solar r-process (Goriely 1999), whereas the continuous blue line corresponds to s-process nucleosynthesis abundance ratio scaling with the predictions from the 5th pulse of a $1.5 M_{\odot}$ star at $[\text{Fe}/\text{H}] = -1$.

4. Classification based on $[\text{Ba}/\text{Eu}]$ and $[\text{La}/\text{Eu}]$ abundance ratios

Various abundance thresholds have been used for the classification of CEMP-s and -rs stars (see discussion in Sect. 5 of

Table 1. Programme stars, adopted atmospheric parameters from K21 and abundance profile distances to the r-process (Sect. 5). ξ is the microturbulence velocity. For the criteria used to classify stars as 'no s-process', 'mild s-process enrichment' and 'strong s-process enrichment', see Sect. 4 of Karinkuzhi et al. (2021b). In the column 'Remark', we identify two stars where a Li abundance could be derived ('Li' if the Li abundance is subsolar and 'Li-rich' if it is super-solar).

Name	T_{eff} (K)	$\log g$ (cm s^{-2})	[Fe/H] (dex)	ξ (km s^{-1})	Signed distance	RMS distance	Remark
no s-process enrichment							
HD 7863	4637 ± 64	2.29 ± 0.40	-0.07 ± 0.05	1.26 ± 0.10	0.37	0.43	
HIP 69788	5127 ± 11	3.90 ± 0.14	-0.04 ± 0.04	0.61 ± 0.10	0.65	0.70	
TYC 3144–1906–1	4136 ± 64	1.89 ± 0.50	-0.13 ± 0.10	1.37 ± 0.04	0.41	0.45	Li
TYC 4684–2242–1	4651 ± 20	2.70 ± 0.14	-0.05 ± 0.07	1.15 ± 0.05	0.28	0.36	
mild s-process enrichment							
BD –07° 402	4654 ± 6	2.62 ± 0.19	-0.11 ± 0.05	1.22 ± 0.10	0.46	0.51	Li-rich
BD +44° 575	4175 ± 6	1.50 ± 0.19	-0.45 ± 0.05	1.60 ± 0.10	0.43	0.47	
TYC 22–155–1	4704 ± 9	3.10 ± 0.32	-0.20 ± 0.10	1.04 ± 0.05	0.20	0.32	
TYC 2913–1375–1	4757 ± 69	2.00 ± 0.30	-0.61 ± 0.11	1.45 ± 0.05	0.24	0.32	
TYC 3305–571–1	4816 ± 3	2.76 ± 0.16	-0.05 ± 0.08	1.31 ± 0.04	0.48	0.53	
TYC 752–1944–1	5069 ± 25	2.94 ± 0.05	-0.08 ± 0.08	1.33 ± 0.04	0.70	0.74	
TYC 4837–925–1	4679 ± 34	2.16 ± 0.29	-0.27 ± 0.07	1.30 ± 0.04	0.37	0.43	
TYC 3423–696–1	5042 ± 64	3.66 ± 0.30	0.02 ± 0.08	0.96 ± 0.04	0.35	0.41	
strong s-process enrichment							
TYC 2250–1047–1	5335 ± 25	3.71 ± 0.18	-0.55 ± 0.12	1.45 ± 0.05	0.56	0.64	
TYC 2955–408–1	4716 ± 64	2.49 ± 0.3	-0.39 ± 0.08	1.25 ± 0.04	0.74	0.79	
TYC 591–1090–1	5267 ± 36	3.68 ± 0.50	-0.30 ± 0.12	1.18 ± 0.06	0.63	0.69	

Table 2. Sensitivity of the abundances ($\Delta \log \epsilon_X$) with variations of the atmospheric parameters (considering the atmospheric parameters of BD –07° 402).

Element	$\Delta \log \epsilon_X$			
	ΔT_{eff} (+100 K)	$\Delta \log g$ (+0.5)	$\Delta [\text{Fe}/\text{H}]$ (+0.5 dex)	$\Delta \xi_t$ (+0.5 km s^{-1})
Nd	0.00	0.13	0.07	0.00
Pr	0.03	0.19	0.22	-0.01
Sm	0.06	0.30	0.15	0.02
Eu	0.05	0.22	0.03	0.06

Karinkuzhi et al. 2021a). In Fig. 2 (resp., Fig. 3), typical (s,r) planes are presented, using lanthanum (resp., barium) as a prototype s-element, and europium as a representative r-element. The different colored regions correspond to commonly accepted limits (Beers & Christlieb 2005) for CEMP-s stars ($[\text{Ba}/\text{Eu}]$ or $[\text{La}/\text{Eu}] > 0.5$, blue region), for CEMP-rI stars ($[\text{Ba}/\text{Eu}]$ or $[\text{La}/\text{Eu}] < 0$, $0 < [\text{Eu}/\text{Fe}] < +1$, light green region), and for CEMP-rII stars ($[\text{Ba}/\text{Eu}]$ or $[\text{La}/\text{Eu}] < 0$, $[\text{Eu}/\text{Fe}] > +1$, dark green region). Finally, the intermediate region between the blue CEMP-s and the green CEMP-r regions has been colored in red. A growing number of stars enriched in both r and s elements (CEMP-rs) has been found in the past decade to occupy this region. In Figs. 2 and 3, CEMP-r, -s and -sr stars from Masseron et al. (2010), Karinkuzhi et al. (2018), Karinkuzhi et al. (2021a) are shown as green, blue and red dots, respectively. In addition, barium stars analyzed by Roriz et al. (2021) (for which the barium abundance is not available) are plotted as small blue crosses in Fig. 2.

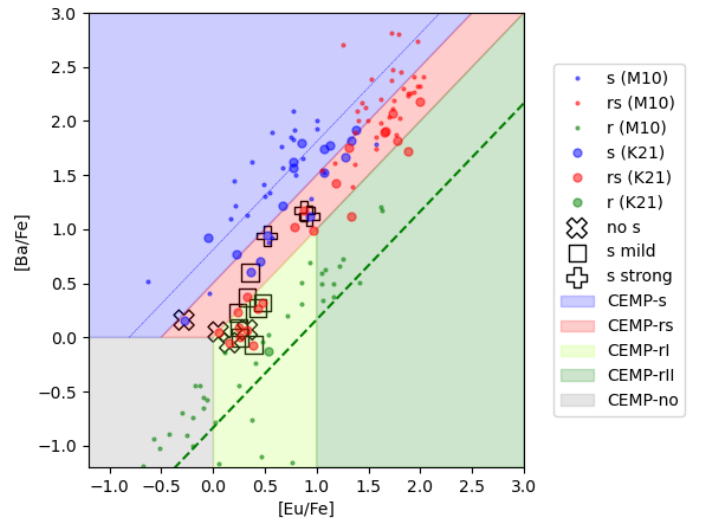


Fig. 3. Same as Fig. 2, but with $[\text{Ba}/\text{Fe}]$ as a function of $[\text{Eu}/\text{Fe}]$.

The majority of barium stars analysed by Roriz et al. (2021) and of CEMP-s stars is located as expected in the blue-shaded region. However, we note that especially at low enrichment levels ($[\text{La}/\text{Fe}]$ and $[\text{Eu}/\text{Fe}] < 0.7$), many barium and CEMP-s stars occupy the red-shaded region. Actually if the enrichment is low, the pristine composition might not be erased by the pollution from the companion and the current abundance profile might also reflect an enrichment due to the Galactic chemical evolution. Al-

ternatively, it can be due to the difficulty to determine weak line abundances in blended spectra¹.

The 15 stars of the current sample are identified in Fig. 2 with black symbols surrounding the corresponding dots: black crosses for the "no s-process enrichment", black squares for the "mild enrichment" and pluses for the "strong enrichment" of Table 1. Interestingly, they all fall in the CEMP-rs (red) or r-I (green) regions. This is reminiscent of the barium stars analyzed by den Hartogh et al. (2022): these authors detect a signature of an i-process activation in about 25% of the evolved companions of the barium star.

5. Classification based on s- and r- elements

We have used 7 elemental abundances (Y, Zr, Ba, La, Ce, Nd, Sm) to compute a signed distance to a reference abundance pattern, chosen as the solar r-process, scaled to the europium abundance of the star (see Eq. 3 of Karinkuzhi et al. 2021a):

$$d_S = \frac{1}{N} \sum_{x_i} (\log_{10} \epsilon_{x_i,*} - \log_{10} \epsilon_{x_i,\text{norm}(r,*)}) \quad (1)$$

where $\{x_1 \dots x_N\}$ are the N considered heavy elements, and we use the usual notation $\log_{10} \epsilon_{x_i} = \log_{10}(n_{x_i}/n_{\text{H}}) + 12$, with n_{x_i} the number density of element x_i . We denote $\log_{10} \epsilon_{x_i,*}$ the abundance of element x_i for the program stars, and $\log_{10} \epsilon_{x_i,\text{norm}(r,*)}$ the standard r-process abundance profile $\log \epsilon_{x_i,r}$ normalized to the star abundance profile with respect to europium:

$$\log \epsilon_{x_i,\text{norm}(r,*)} = \log \epsilon_{x_i,r} + (\log \epsilon_{Eu,*} - \log \epsilon_{Eu,r}), \quad (2)$$

where the adopted r-process abundances $\log \epsilon_{x_i,r}$ are listed in Table B.4 of Karinkuzhi et al. (2021a). Figure 4 presents the histogram of this signed distance, together with the limit adopted in Karinkuzhi et al. (2021a) to separate CEMP-s from CEMP-rs stars (at $d_S = 0.6$). This limit is certainly somewhat arbitrary. However, Fig. 4 shows that most of our sample stars strongly enriched in heavy elements appear to have an rs pattern.

6. Comparison with nucleosynthesis predictions

AGB nucleosynthesis predictions have been computed coupling the STAREVOL code (Siess & Arnould 2008) with an extended reaction network of 1160 species linked by 2123 nuclear reactions. More details on the nuclear network and input physics can be found in Choplin et al. (2021) and Goriely et al. (2021). The solar abundances are taken from Asplund et al. (2009) which correspond to a metallicity $Z = 0.0134$. The Reimers (1975) mass loss rate with $\eta_R = 0.4$ is used from the main sequence up to the end of core helium burning and the Vassiliadis & Wood (1993) during the AGB phase. Dedicated models with an initial mass of $2 M_{\odot}$ and a metallicity of $[\text{Fe}/\text{H}] = -0.5$, close to the one derived from the observations, have been computed as explained below.

In the present calculations, a diffusion equation is used to compute the partial mixing of protons in the C-rich layers at the time of the third dredge-up (TDU). We follow Eq. (9) of Goriely & Siess (2018) and use in our standard case the same diffusive mixing parameters in our simulations as in Shetye et al. (2019), *i.e.*, $f_{\text{env}} = 0.14$, $D_{\text{min}} = 10^7 \text{ cm}^2 \text{ s}^{-1}$ and $p = 1/2$, where f_{env} controls the extent of the mixing, D_{min} the value of the diffusion

¹ We do not consider stars with low enrichment levels ($[\text{X}/\text{Fe}] < 0.2$ dex) as barium stars, given the typical uncertainties affecting the abundance determinations.

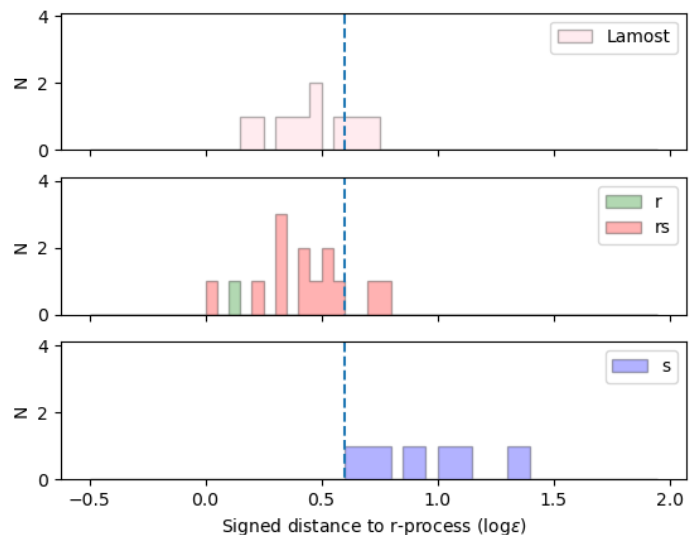


Fig. 4. *Upper panel:* Histogram of the signed distance (Eq. 1) of the star sample of the present study (considering only those with mild and strong enrichments, so 11 stars out of 15). *Middle panel:* Same histogram for the Karinkuzhi et al. (2018) sample of CEMP-rs (red) and -r (green) stars. *Lower panel:* Same histogram for the Karinkuzhi et al. (2018) sample of CEMP-s stars. The dashed line represents the $d_S = 0.6$ limit between CEMP-s and CEMP-rs stars, as defined in Karinkuzhi et al. (2021a).

coefficient at the base of the envelope, and p is a free parameter describing the shape of the diffusion profile. In addition to this diffusive mixing at the base of the envelope, a similar prescription is applied at the top of the thermal pulse where a coefficient f_{pulse} governs the diffusive transport. Two different values of the f_{pulse} coefficient, triggering an s-process or i-process nucleosynthesis, are considered here, as explained below.

When considering a relatively weak diffusive mixing at the top of the thermal pulse characterized by $f_{\text{pulse}} = 0.03$, the AGB phase of our $2 M_{\odot}$ $[\text{Fe}/\text{H}] = -0.5$ model star is found to follow a standard evolution with the occurrence of 8 thermal pulses and a regular surface enrichment at the time of the TDU. In addition, the diffusive mixing at the bottom of the envelope gives rise to a radiative s-process during the interpulse phases similar to what is found in Goriely & Siess (2018). The corresponding abundance pattern found at the surface at the end of the AGB evolution is illustrated in Fig. 5 (blue curve).

The ingestion of protons in the convective helium-burning zone can lead to a rich i-process nucleosynthesis that can explain quite successfully the surface enrichment of CEMP-rs stars (e.g. Hampel et al. 2019; Karinkuzhi et al. 2021a; Choplin et al. 2021). However, as detailed in Choplin et al. (2022), when no extra mixing is included, the proton ingestion event (PIE) is restricted to model stars of metallicity lower than typically $[\text{Fe}/\text{H}] \sim -2$. When considering diffusive mixing below the envelope and at the top of the thermal pulse, it is found that a possible PIE can be triggered in a way very similar to those found in very metal-poor stars. In particular, mixing parameters $f_{\text{env}} = 0.06$ and $f_{\text{pulse}} = 0.06$ lead to a PIE at the time of the third thermal pulse, with a maximum neutron density reaching 10^{14} cm^{-3} . The resulting surface abundance distribution is shown in Fig. 5 (red profile) and is rather similar to the one obtained in low-metallicity stars (Choplin et al. 2022).

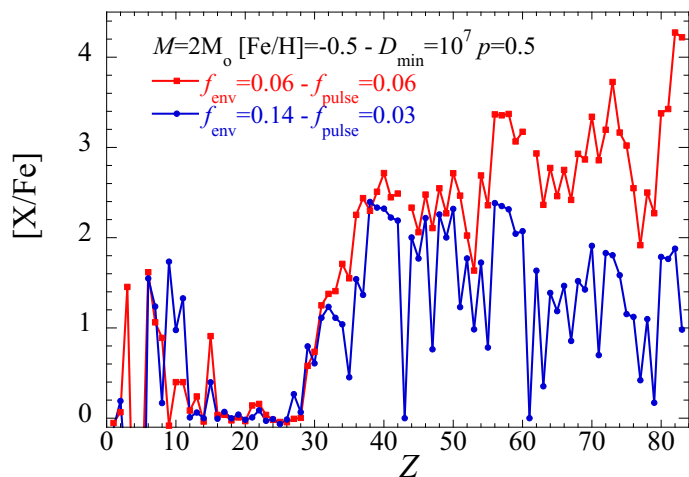


Fig. 5. Comparison of the final elemental surface distributions $[X/Fe]$ (solid lines) obtained after the development of the neutron-capture processes in a $2 M_{\odot}$ AGB star of metallicity $[Fe/H] = -0.5$. The blue line is obtained with a diffusive mixing characterized by $f_{env} = 0.14$ and $f_{pulse} = 0.03$ and give rise to an s-process nucleosynthesis while the red line results from a mixing with $f_{env} = 0.06$ and $f_{pulse} = 0.06$ leading to a PIE, i.e., to an i-process nucleosynthesis.

In summary, depending on the strength of the overshoot mixing imposed both at the bottom of the envelope and at the top of the pulse, either a standard s-process or an i-process can be simulated in a $2 M_{\odot}$ $[Fe/H] = -0.5$ model star. Despite progress in multi-dimensional simulations of convective boundary mixing (e.g., in low-mass stars, Mocák et al. 2011; Herwig et al. 2014; Woodward et al. 2015), no firm conclusion can be drawn on the strength of the mixing. Our approach is to explore these possibilities and compare our results with the present observations.

A particular attention is paid to the most strongly enriched s-process stars of Table 1, because their abundances must reflect a genuine pollution and not the chemical enrichment of the Galaxy, contrarily to the situation that might prevail for stars with low-enrichments. In particular, TYC 2250-1047-1 and TYC 591-1090-1 have $[Eu/Fe]$ of 0.88 and 0.93 dex, respectively, which cannot be explained by galactic chemical evolution alone. Virtually no star is found with $[Eu/Fe] > 0.4$ among disk stars with $[Fe/H] > -0.4$ (Tautvaišienė et al. 2021; Van der Swaelmen et al. 2023). Therefore the abundance pattern of these two stars must result from extra pollution(s). TYC 2955-408-1, with $[Eu/Fe] = 0.52$, is difficult to classify and the abundance of additional elements is needed to decide whether it is an i-process star or a barium star with a europium abundance corresponding to the high-europium tail of the Galactic distribution. A comparison of their measured and predicted abundances is given in Fig. 6 where a dilution factor is applied to the surface abundances shown in Fig. 5 to match the overabundances observed in the La-Ba region. This dilution factor is required to simulate the mixing of the nucleosynthesis yields from the primary star onto its companion (assumed to be of the same initial composition).

The overall accuracy of the model predictions can be quantified for each star through the reduced χ^2 indicator:

$$\chi^2 = \frac{1}{N} \sum_X \frac{([X/Fe]_{obs} - [X/Fe]_{mod})^2}{\sigma_{X,obs}^2}, \quad (3)$$

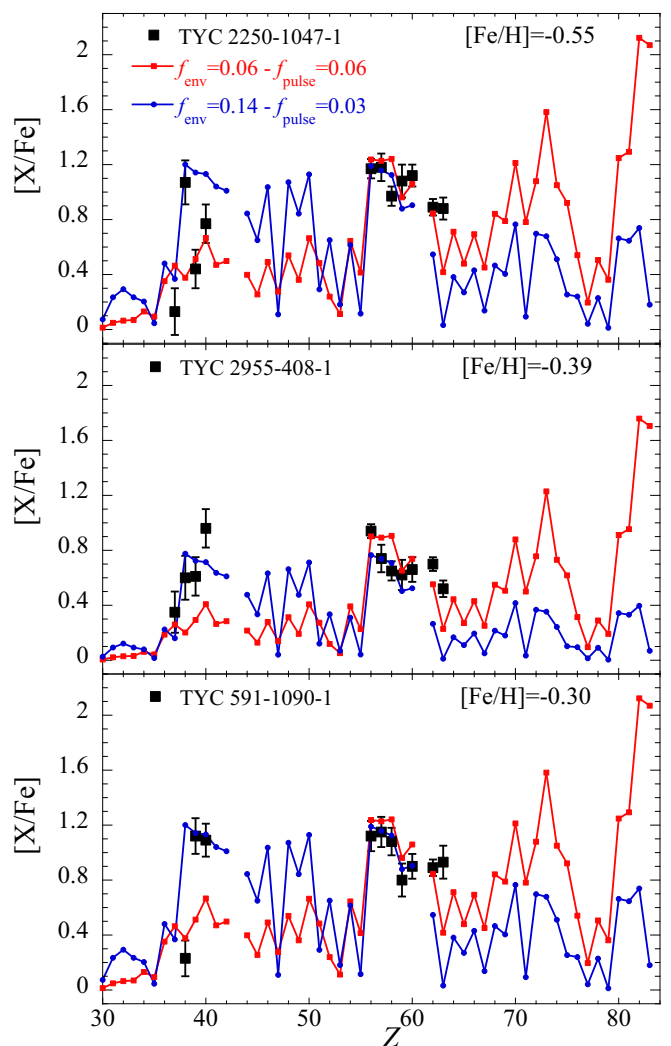


Fig. 6. Comparison of the measured abundances with nucleosynthesis predictions from the STAREVOL code. The abundances obtained at the surface of the $2 M_{\odot}$ $[Fe/H] = -0.5$ model with two different sets of the diffusive mixing parameters, (the blue line corresponding to an s-process, and the red line to an i-process) as shown in Fig. 5, are compared with the abundances of the 3 most enriched barium stars (black squares).

where $[X/Fe]_{obs}$ and $[X/Fe]_{mod}$ are respectively the measured and predicted abundances of a given element X and $\sigma_{X,obs}$ is the associated uncertainty on the measured abundance. We consider the $N = 10$ elements available in all stars, namely Sr, Y, Zr, Ba, La, Ce, Pr, Nd, Sm, and Eu.

We report a typo in Eq. 6 of Karinkuzhi et al. (2021a), where the normalizing factor $1/N$ was erroneously omitted, though it was included when computing the χ^2 listed in the Table 1 of that paper (see Corrigendum in Karinkuzhi et al. 2023). Equation 3 above is the correct expression used to provide the numbers given in the tables of both papers.

In Karinkuzhi et al. (2021a), reduced χ^2 values for CEMP-s stars (when compared to an s-process) ranged between 2.7 and 10.9. Similarly, reduced χ^2 values for CEMP-rs stars (when compared to an i-process) ranged between 1.3 and 10.6. Here, for the two most-enriched stars (TYC 2250-1047-1 and TYC 591-

Table 3. Reduced χ^2 computed either (i) on the same 7 elements (Y, Zr, Ba, La, Ce, Nd, Sm) as for the signed or RMS distances (where Eu is used as a normalizing element), (ii) based on the previous elements plus Eu and (iii) based on the 10 elements (Sr, Y, Zr, Ba, La, Ce, Pr, Nd, Sm, and Eu) with derived abundances in the present paper. For convenience, the signed distance (Eq. 1) and the RMS distance (Eq. 4 of Karinkuzhi et al. 2021a) are repeated in the last two columns.

Name, Number of elements	Reduced χ^2		Distance	
	s-pro	i-pro	d_S	d_{RMS}
TYC 2250-1047-1				
7	10.9	2.6	0.56	0.64
8	23.7	6.5		
10	19.3	7.1		
TYC 591-1090-1				
7	4.8	6.0	0.63	0.69
8	11.2	7.6		
10	14.6	6.4		

1090-1), we find reduced χ^2 between 6.4 and 7.6 (depending on the exact number (8 or 10) of considered chemical elements, but including Eu, see Table 3) when comparing to an i-process, but in the range between 11.2 and 23.7 when comparing to an s-process. Hence the chemical pattern of these two most-enriched stars is better reproduced by an i-process than by an s-process.

We note that the first peak s-process element abundances (Sr, Y, Zr) are always difficult to reproduce (either by an s- or i-process, Fig. 6), and this strongly impacts the χ^2 . The results from the χ^2 are thus less clear with the 7 elements than with a metric using 8 (i.e. including Eu) or 10 elements (including Sr, Pr and Eu). Considering Eu in addition to Sm is thus crucial when assessing an i- or r- contribution. We note that among these two stars, only TYC 2250-1047-1 is classified as rs-enriched according to the signed distance criterion ($d_S < 0.6$). The reason partially lies in the fact that the 0.6 threshold on the signed distance is a somewhat arbitrary value and, as seen in Fig. 4, values up to $d_S = 0.75$ might still be encountered for some CEMP-rs stars falling in the intermediate (red) regions of Fig. 2 and 3.

In summary, in this paper we use two different indicators to assess the s- or i-character of a measured stellar abundance profile: the distance indicator (using 7 heavy elements plus Eu which serves to normalize the measured Eu abundance to the solar-scaled "universal" r-process abundance; it has the advantage to be model-independent) and the reduced χ^2 (computed between the measured profile and a nucleosynthetic predictions, either s or i). Table 3 shows that these two indicators are consistent when the comparison is based on the same set of chemical elements, as can be seen by comparing the reduced χ^2 for 7 elements (6.0, 2.6) and the d_S distance which uses the same 7 elements (0.63, 0.56) for the two stars (TYC 591-1090-1, TYC 2250-1047-1), ordered by increasing contribution of an i-process. The 8 and 10-element χ^2 show that including Sr as well as Pr and Eu is very important to get clearly different s process χ^2 and i-process χ^2 , and thus to get a clear diagnostic concerning the s- or rs-character of the abundance profile.

We demonstrate in the next section that replacing the i-process pattern with any superposition of two independent s- and r-pollutions deteriorates the agreement with the measured abundances.

7. Testing the two independent pollutions scenario

To check that the two i-process star (TYC 2250-1047-1 and TYC 591-1090-1) abundance patterns are better fitted with an i-process than with a superposition of two independent pollutions, one by an s-process and another one by an r-process, we performed the following test. A mixed r+s profile was added to a solar abundance profile scaled to the metallicity of the considered star. The r+s profile was built summing an r- and an s-contribution, each one varied independently from zero value to values producing overabundances largely exceeding the measured abundances. We assume a solar-like pattern for the r-process (Table B.4 of Karinkuzhi et al. 2021a) and an AGB pattern for the s-process at the corresponding stellar metallicity (blue line in Fig. 6; see also Goriely & Siess 2018). The agreement between the resulting abundance profile (plotted in faded colors in Fig. 7) and the measured profile was quantified by computing a χ^2 as in Eq. 3. For the two stars, a pure s-process produces a better agreement with the measured abundances than a r+s mixture. An r-process contribution is never favored because the slope of the r-process is quite steep (i.e., it is more rapidly decreasing with increasing Z than the s-process), so matching the high europium (as well as samarium) abundances would inevitably lead to a large overestimate of the light-s (Sr, Y, Zr) abundances. The resulting χ^2_s (between the s-profile and the measured abundances) is very similar to the χ^2_i (between the i-profile and the measured abundances), but the s-profile never explains the high europium abundance measured in TYC 2250-1047-1 and TYC 591-1090-1. The present analysis indicates that these two enriched stars are better explained by an i-process than by a superposition of two independent s and r processes.

Some deviations between the measured and i-process abundances can still be noted, in particular for light s-elements, but also for Eu, which, in contrast to Sm, tends to be underestimated by the model. The absence of odd-even effect between measured Sm-Eu abundance is puzzling.

8. Conclusions

Our re-analysis of fifteen stars classified as s-process-enriched by Norfolk et al. (2019) indicates that their abundances seem to be rather characterized by a hybrid sr pattern, rather than by a pure s-process pattern, as inferred from the distance indicator (d_S) that quantifies the deviation of the star's abundance profile from a pure r-process distribution. For the two most enriched stars of our sample (that have $[Eu/Fe] \gtrsim 0.75$ and that cannot be explained by Galactic chemical evolution models) the comparison of the abundance profile with detailed calculations show that an i-process nucleosynthesis (resulting from the occurrence of a PIE) fits better the observed abundances than a pure s-process or than any combination of r- and s-patterns. At low-enrichment levels, the primordial composition resulting from the galactic chemical evolution blurs the picture. This can be seen in Fig. 2, where the barium stars enter the r+s region below $[s/Fe]=0.5$ dex.

It is possible that a non-negligible fraction of the stars previously identified as barium stars (because barium enhancement is relatively easy to identify) also present an r-element enrichment, but it is only recently that r-element abundances have been systematically investigated among barium stars. A population of rs-enriched objects (with $[La/Eu] < 0.5$) seems to emerge, not only at low-metallicities where it was first noticed (among CEMP-rs stars), but also at close-to-solar metallicities, as also found in other samples of barium stars (Karinkuzhi et al. 2018; den Har-

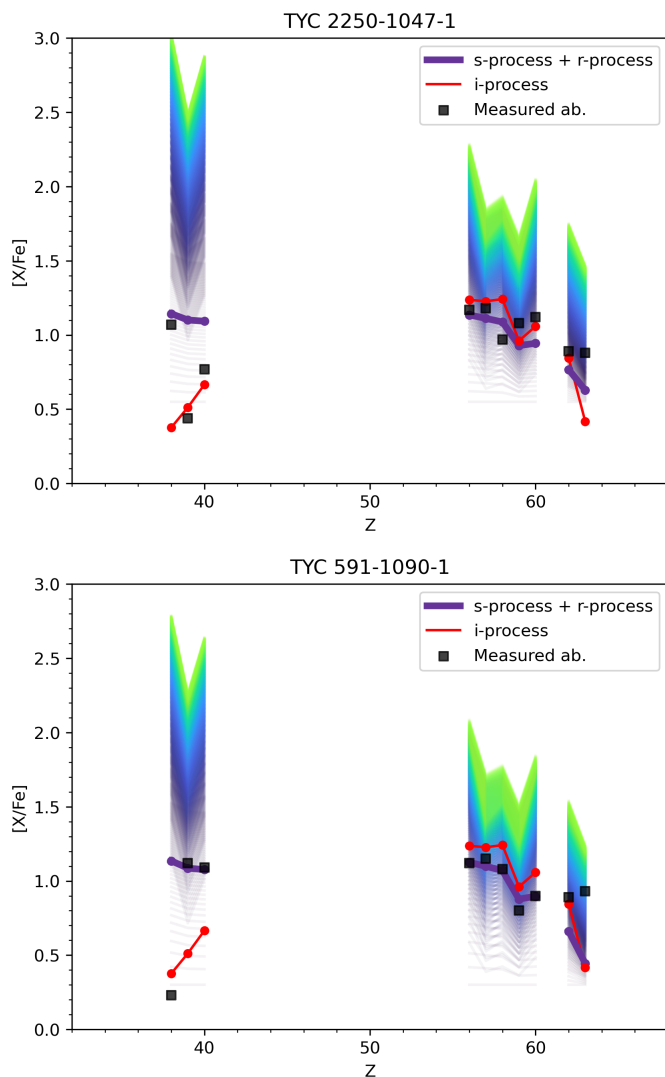


Fig. 7. Comparison of the measured abundance profiles (black squares) with a series of synthetic profiles made by a superposition of s- (as plotted in Fig. 6) and r-process profiles, both varied independently and continuously from a solar-scaled profile with a very low s+r enrichment (purple faded lines) to large s+r enrichments (green faded lines). The synthetic "s+r" profile best matching the measured abundances is plotted as a thick violet line. For both stars it actually corresponds to a pure s-process contribution (hence any r-process contribution would deteriorate the agreement, whatever the s-process contribution). For reference, the i-process profile best matching the measured abundances is plotted in red as in Fig. 6.

togh et al. 2022) and in Sakurai's object (Herwig et al. 2011; van Hoof et al. 2017). If the i-process is indeed active in objects like AGB stars of close-to-solar metallicity, important impact on nucleosynthesis and galactic chemical evolution can be expected. In particular, the i-process contribution to our solar system would need to be revisited.

Acknowledgements. D.K. acknowledges the financial support from University of Calicut through seed money grant. SVE thanks the Fondation ULB for its support. The *Mercator* telescope is operated thanks to grant number G.0C31.13 of the FWO under the "Big Science" initiative of the Flemish government. Based on observations obtained with the HERMES spectrograph, supported by the Fund for Scientific Research of Flanders (FWO), the Research Council of K.U.Leuven, the Fonds National de la Recherche Scientifique (F.R.S.- FNRS), Belgium, the Royal Observatory of Belgium, the Observatoire de Genève, Switzerland and the Thüringer Landessternwarte Tautenburg, Germany. LS and

SG are senior research associates from F.R.S.- FNRS (Belgium). This work was supported by the F.R.S.- FNRS Grant No IISN 4.4502.19.

References

- Alvarez, R. & Plez, B. 1998, *A&A*, 330, 1109
 Asplund, M., Grevesse, N., Sauval, A. J., & Scott, P. 2009, *ARA&A*, 47, 481
 Beers, T. C. & Christlieb, N. 2005, *ARA&A*, 43, 531
 Choplin, A., Siess, L., & Goriely, S. 2021, *A&A*, 648, A119
 Choplin, A., Siess, L., & Goriely, S. 2022, *A&A*, 667, A155
 Cui, W. Y., Zhang, B., Shi, J. R., et al. 2014, *A&A*, 566, A16
 den Hartogh, J. W., Yagüe López, A., Cseh, B., et al. 2022, *A&A* (in press), arXiv:2212.03593
 Goriely, S. 1999, *A&A*, 342, 881
 Goriely, S. & Siess, L. 2018, *A&A*, 609, A29
 Goriely, S., Siess, L., & Choplin, A. 2021, *A&A*, 654, A129
 Hampel, M., Karakas, A. I., Stancliffe, R. J., Meyer, B. S., & Lugaro, M. 2019, *ApJ*, 887, 11
 Hampel, M., Stancliffe, R. J., Lugaro, M., & Meyer, B. S. 2016, *ApJ*, 831, 171
 Heiter, U. 2020, in *IAU General Assembly*, 458–462
 Heiter, U., Lind, K., Asplund, M., et al. 2015, *Phys. Scr.*, 90, 054010
 Herwig, F., Pignatari, M., Woodward, P. R., et al. 2011, *ApJ*, 727, 89
 Herwig, F., Woodward, P. R., Lin, P.-H., Knox, M., & Fryer, C. 2014, *ApJ*, 792, L3
 Jonsell, K., Barklem, P. S., Gustafsson, B., et al. 2006, *A&A*, 451, 651
 Karinkuzhi, D., Van Eck, S., Goriely, S., et al. 2021a, *A&A*, 645, A61
 Karinkuzhi, D., Van Eck, S., Goriely, S., et al. 2023, *A&A*, 671, C8
 Karinkuzhi, D., Van Eck, S., Jorissen, A., et al. 2021b, *A&A*, 654, A140
 Karinkuzhi, D., Van Eck, S., Jorissen, A., et al. 2018, *A&A*, 618, A32
 Mashonkina, L. & Christlieb, N. 2014, *A&A*, 565, A123
 Mashonkina, L. I., Shimanskiĭ, V. V., & Sakhibullin, N. A. 2000, *Astronomy Reports*, 44, 790
 Masseron, T., Johnson, J. A., Plez, B., et al. 2010, *A&A*, 509, A93
 Mocaĭk, M., Siess, L., & Müller, E. 2011, *A&A*, 533, A53
 Norfolk, B. J., Casey, A. R., Karakas, A. I., et al. 2019, *MNRAS*, 490, 2219
 Raskin, G., van Winckel, H., Hensberge, H., et al. 2011, *A&A*, 526, A69
 Reimers, D. 1975, *Mémoires of the Société Royale des Sciences de Liège*, 8, 369
 Roriz, M. P., Lugaro, M., Pereira, C. B., et al. 2021, *MNRAS*, 507, 1956
 Shetye, S., Goriely, S., Siess, L., et al. 2019, *A&A*, 625, L1
 Siess, L. & Arnould, M. 2008, *A&A*, 489, 395
 Tautvaišienė, G., Viscasillas Vázquez, C., Mikolaitis, Š., et al. 2021, *A&A*, 649, A126
 Van der Swaelmen, M., Viscasillas Vázquez, C., Cescutti, G., et al. 2023, *A&A*, 670, A129
 van Hoof, P. A. M., Herwig, F., Kimeswenger, S., et al. 2017, *Mem. Soc. Astron. Italiana*, 88, 463
 Vassiliadis, E. & Wood, P. R. 1993, *ApJ*, 413, 641
 Woodward, P. R., Herwig, F., & Lin, P.-H. 2015, *ApJ*, 798, 49

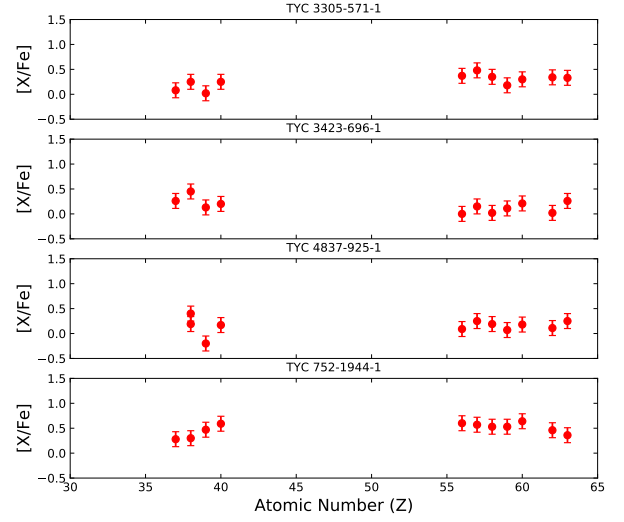
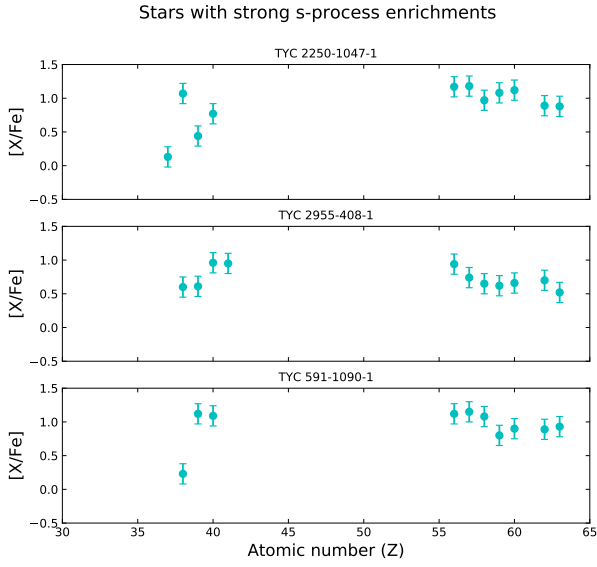
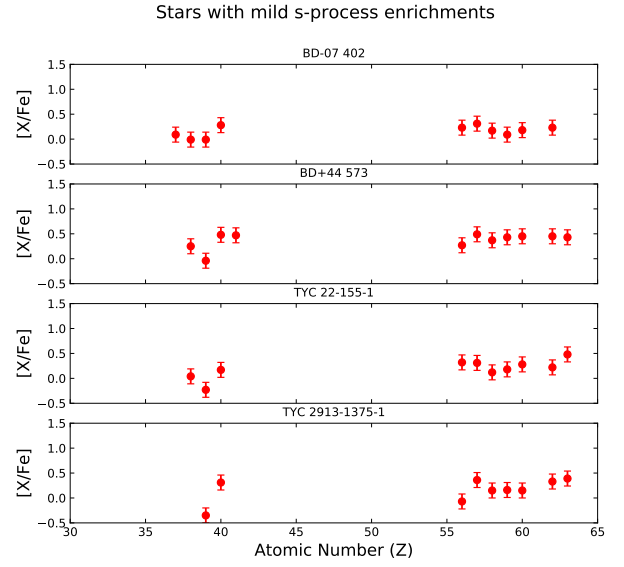
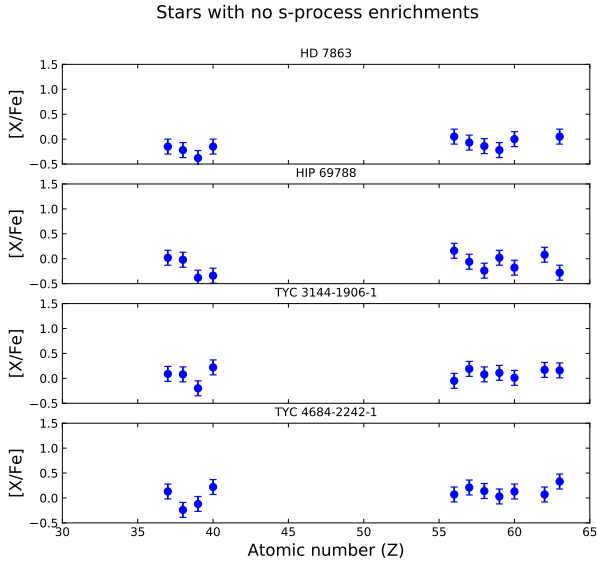


Fig. B.1. Abundance profiles of the program stars color - coded according to the adopted classification criteria. The upper panel shows the abundance pattern in stars with no s-process enhancements. The lower panel shows the the abundance pattern in three stars with strong s-process enrichments.

Fig. B.2. Same as B.1 but for the the eight mild s-process enriched stars.

Appendix A: Individual abundances

Table A.1 lists the elemental abundances.

Appendix B: Abundance pattern in program stars

Fig. B.1 and B.2 show the abundance patterns for stars showing no, mild or strong s-process enrichments. Figure 3 displays the ([Ba/Fe], [Eu/Fe]) diagram.

Table A.1. Elemental abundances

		BD -07°402				BD +44°575			HD 7863		
Z	$\log_{\odot}\epsilon^a$	$\log\epsilon$	σ_l (N)	$[X/Fe] \pm \sigma_t$	$\log\epsilon$	σ_l (N)	$[X/Fe] \pm \sigma_t$	$\log\epsilon$	σ_l (N)	$[X/Fe] \pm \sigma_t$	
Pr II	59	0.72	0.70	0.10(3)	0.09 ± 0.12	0.70	0.10(1)	0.43 ± 0.14	0.43	0.03(2)	-0.22 ± 0.10
Nd II	60	1.42	1.49	0.09(8)	0.18 ± 0.08	1.42	0.06(7)	0.45 ± 0.08	1.35	0.08(6)	0.00 ± 0.08
Sm II	62	0.96	1.08	0.10(5)	0.23 ± 0.05	0.96	0.06(4)	0.45 ± 0.05			
Eu II	63	0.52	0.65	0.10(2)	0.24 ± 0.09	0.50	0.10(2)	0.43 ± 0.09	0.50	0.10(4)	0.05 ± 0.08
		HIP 69788				TYC 22-155-1			TYC 2250-1047-1		
Z	$\log_{\odot}\epsilon^a$	$\log\epsilon$	σ_l (N)	$[X/Fe] \pm \sigma_t$	$\log\epsilon$	σ_l (N)	$[X/Fe] \pm \sigma_t$	$\log\epsilon$	σ_l (N)	$[X/Fe] \pm \sigma_t$	
Pr II	59	0.72	0.70	0.10(1)	0.02 ± 0.14	0.70	0.10(3)	0.18 ± 0.12	1.15	0.10(3)	1.08 ± 0.12
Nd II	60	1.42	1.20	0.10(3)	-0.18 ± 0.10	1.55	0.06(7)	0.28 ± 0.08	1.99	0.09(13)	1.12 ± 0.08
Sm II	62	0.96	1.00	0.10(3)	0.08 ± 0.09	0.98	0.04(5)	0.22 ± 0.05	1.30	0.10(4)	0.89 ± 0.06
Eu II	63	0.52	0.20	0.10(2)	-0.28 ± 0.09	0.80	0.10(2)	0.48 ± 0.09	0.85	0.08(3)	0.88 ± 0.08
		TYC 2913-1375-1				TYC 2955-408-1			TYC 3144-1906-1		
Z	$\log_{\odot}\epsilon^a$	$\log\epsilon$	σ_l (N)	$[X/Fe] \pm \sigma_t$	$\log\epsilon$	σ_l (N)	$[X/Fe] \pm \sigma_t$	$\log\epsilon$	σ_l (N)	$[X/Fe] \pm \sigma_t$	
Pr II	59	0.72	0.27	0.05(3)	0.16 ± 0.11	0.95	0.04(3)	0.62 ± 0.11	0.70	0.10(2)	0.11 ± 0.13
Nd II	60	1.42	0.96	0.08(9)	0.15 ± 0.08	1.69	0.13(7)	0.66 ± 0.09	1.30	0.03(9)	0.01 ± 0.08
Sm II	62	0.96	0.68	0.12(6)	0.33 ± 0.06	1.27	0.05(7)	0.70 ± 0.05	1.00	0.20(6)	0.17 ± 0.09
Eu II	63	0.52	0.30	0.10(2)	0.39 ± 0.09	0.65	0.05(2)	0.52 ± 0.06	0.55	0.07(3)	0.16 ± 0.07
		TYC 3305-571-1				TYC 3423-6966-1			TYC 4684-2242-1		
Z	$\log_{\odot}\epsilon^a$	$\log\epsilon$	σ_l (N)	$[X/Fe] \pm \sigma_t$	$\log\epsilon$	σ_l (N)	$[X/Fe] \pm \sigma_t$	$\log\epsilon$	σ_l (N)	$[X/Fe] \pm \sigma_t$	
Pr II	59	0.72	0.85	0.15(2)	0.18 ± 0.15	0.85	0.10(1)	0.11 ± 0.14	0.70	0.10(2)	0.03 ± 0.12
Nd II	60	1.42	1.67	0.05(3)	0.30 ± 0.09	1.65	0.10(6)	0.21 ± 0.09	1.50	0.10(6)	0.13 ± 0.09
Sm II	62	0.96	1.25	0.05(3)	0.34 ± 0.05	1.00	0.05(3)	0.02 ± 0.05	0.98	0.04(5)	0.07 ± 0.05
Eu II	63	0.52	0.80	0.10(2)	0.33 ± 0.09	0.80	0.10(1)	0.26 ± 0.12	0.80	0.10(2)	0.33 ± 0.09
		TYC 4837-925-1				TYC 591-1090-1			TYC 752-1944-1		
Z	$\log_{\odot}\epsilon^a$	$\log\epsilon$	σ_l (N)	$[X/Fe] \pm \sigma_t$	$\log\epsilon$	σ_l (N)	$[X/Fe] \pm \sigma_t$	$\log\epsilon$	σ_l (N)	$[X/Fe] \pm \sigma_t$	
Pr II	59	0.72	0.52	0.06(3)	0.07 ± 0.09	1.30	0.10(3)	0.80 ± 0.12	1.17	0.09(3)	0.53 ± 0.12
Nd II	60	1.42	1.33	0.12(7)	0.18 ± 0.09	2.02	0.14(8)	0.90 ± 0.09	1.98	0.05(9)	0.64 ± 0.08
Sm II	62	0.96	0.80	0.12(4)	0.11 ± 0.07	1.55	0.09(4)	0.89 ± 0.06	1.34	0.10(8)	0.46 ± 0.05
Eu II	63	0.52	0.50	0.10(2)	0.25 ± 0.09	1.15	0.10(1)	0.93 ± 0.12	0.80	0.10(2)	0.36 ± 0.09

^a Asplund et al. (2009)

: Uncertain abundances due to noisy/blended region